
DATA-DRIVEN SYNTHESIS OF MAGNETIC RESONANCE SPECTROSCOPY DATA USING A VARIATIONAL AUTOENCODER *

Dennis M.J. van de Sande

Department of Biomedical Engineering
Eindhoven University of Technology
Eindhoven, The Netherlands
d.m.j.v.d.sande@tue.nl

Julian P. Merkofer

Department of Electrical Engineering
Eindhoven University of Technology
Eindhoven, The Netherlands

Sina Amirrajab

Department of Biomedical Engineering
Eindhoven University of Technology
Eindhoven, The Netherlands

Mitko Veta

Department of Biomedical Engineering
Eindhoven University of Technology
Eindhoven, The Netherlands

Gerhard S. Drenthen

Department of Radiology & Nuclear Medicine
Maastricht University Medical Center
Maastricht, The Netherlands

Jacobus F.A. Jansen

Department of Electrical Engineering
Eindhoven University of Technology
Eindhoven, The Netherlands
& Department of Radiology & Nuclear Medicine
Maastricht University Medical Center
Maastricht, The Netherlands

Marcel Breeuwer

Department of Biomedical Engineering
Eindhoven University of Technology
Eindhoven, The Netherlands
& Department of Electrical Engineering
Eindhoven University of Technology
Eindhoven, The Netherlands

ABSTRACT

The development of deep learning methods for magnetic resonance spectroscopy (MRS) is often hindered by the limited availability of large, high-quality training datasets. While physics-based simulations are commonly used to mitigate this limitation, accurately modeling all in-vivo signal components remains challenging. In this work, we propose a data-driven framework for synthesizing in-vivo MRS data using a variational autoencoder (VAE) trained exclusively on measured single-voxel spectroscopy data. The model learns a low-dimensional latent representation of complex-valued spectra and enables the generation of new samples through latent-space sampling and interpolation strategies. The generative performance of the proposed approach is evaluated using a comprehensive set of complementary analyses, including reconstruction quality, feature-level similarity using low-dimensional embeddings, application-based signal quality metrics, and metabolite quantification agreement. The results demonstrate that the VAE accurately reconstructs dominant spectral patterns and generates synthetic spectra that occupy the same feature space as in-vivo data. In an example application targeting GABA-edited spectroscopy, augmenting limited subsets of transients with synthetic spectra improves signal quality metrics such as signal-to-noise ratio, linewidth, and

*Pre-print: This manuscript has not been peer-reviewed.

shape scores. However, the results also reveal limitations of the generative approach, including under-representation of stochastic noise and reduced accuracy in absolute metabolite quantification, particularly for applications sensitive to concentration estimates. These findings highlight both the potential and the limitations of data-driven MRS synthesis. Beyond the proposed model, this study introduces a structured evaluation framework for generative MRS methods, emphasizing the importance of application-aware validation when synthetic data are used for downstream analysis.

Keywords Magnetic Resonance Spectroscopy · Variational Autoencoder · Generative Models · Synthetic Data

1 Introduction

Artificial intelligence (AI) and deep learning (DL) are increasingly being adopted in the field of MRS to perform a wide range of tasks, including spectral reconstruction, artifact removal, quantification, classification, and other applications [1, 2]. However, the development of DL-based methods typically requires large amounts of high-quality training data. In MRS, the availability of such data is limited due to the time-consuming nature of acquisitions, high acquisition costs, privacy concerns, and the lack of large open-source databases. This is partly because MRS is not routinely included in clinical imaging protocols.

To mitigate this data scarcity, researchers often rely on model-based MRS simulations to generate artificial training data. Several toolboxes have been developed for this purpose [3, 4, 5, 6, 7], most of which employ reverse-fitting approaches, whereby fitting parameters are provided to the signal model to synthesize spectra rather than being estimated from measured data. While metabolite signals can be accurately simulated using the density matrix formalism [8], other signal contributions, such as macromolecular background signals, residual water, lipids, and additional in-vivo nuisance components, remain challenging to model accurately. Incomplete or simplified modeling of these contributions may result in synthetic spectra that only partially capture the variability observed in practice, leading to domain shift and reduced generalization of DL models trained on such data. Moreover, there is no broadly accepted consensus on the most appropriate signal models or parameter ranges for generating realistic MRS data, which has led to complex, simulation pipelines that are typically not publicly available, thereby hampering independent validation and reproducibility.

As an alternative to physics-based simulations, MRS data can also be generated using data-driven synthesis approaches. These methods leverage existing datasets to train generative models that learn the underlying data distribution, enabling the generation of new spectra without explicitly defining parameter ranges or complex forward models. Generative AI techniques have been applied to various spectroscopy modalities [9]; nevertheless, only a limited number of studies have investigated their application to in-vivo MRS. One example is the work by Maruyama et al. [10], who proposes a generative adversarial network (GAN)-based framework for generating magnetic resonance spectroscopic imaging (MRSI) data using complementary MRI and single voxel spectroscopy (SVS) information. Other studies employing GAN architectures include the work by Olliverre et al. [11], which focused on generating SVS data for different brain tumor grades and evaluated the synthetic spectra using a downstream classification task, as well as the study by Jang et al. [12], which applied GAN-based models for anomaly detection. Notably, in the latter study, the model was trained exclusively on simulated data.

To date, generative AI approaches for MRS have predominantly relied on GAN-based models, while alternative generative frameworks, such as variational autoencoders (VAEs) [13], remain largely unexplored. In contrast to GANs, VAEs provide a probabilistic generative framework with a structured latent space, which has been shown to facilitate the synthesis of realistic medical data and support data augmentation in various imaging domains, including segmentation and classification tasks [14, 15]. Furthermore, there is currently no standardized or widely accepted framework for evaluating the realism and validity of synthetic MRS data, with existing studies employing heterogeneous and application-specific evaluation strategies. Therefore, the aim of this study is to develop a VAE-based framework for generating synthetic SVS MRS data using exclusively in-vivo data. In this work, the framework is developed and evaluated using in-vivo proton brain MRS data. In addition, the generated spectra are systematically evaluated using multiple complementary strategies, including metric-based comparisons, feature similarity analysis, quantification agreement, and application-based evaluations.

2 Materials & Methods

2.1 Data

The dataset used in this study is SVS MRS data acquired from a subcohort of The Maastricht Study dataset [16], and is previously used in van Bussel et al. [17]. The Maastricht Study was approved by the Medical Ethics Committee of the Maastricht University Medical Center+ (Maastricht, the Netherlands), and all participants provided written

informed consent. The dataset used in this study comprises 102 subjects in total. The mean age across all participants is 62.2 ± 8.0 years, with 59 men and 43 women. The cohort is divided into three groups: healthy controls (Group C, $N = 41$, age 59.3 ± 9.0 years, 15 men/26 women), patients with type 2 diabetes (Group D, $N = 44$, age 64.8 ± 6.0 years, 33 men/11 women), and patients with metabolic syndrome (Group M, $N = 17$, age 62.6 ± 8.0 years, 11 men/6 women). More details on the patient population can be found in van Bussel et al. [17].

MRS data is acquired using a 3T scanner (Achieva TX, Philips Healthcare, Best, The Netherlands) and a Mescher-Garwood-point resolved spectroscopy (MEGA-PRESS) sequence (TR/TE = 2000/68ms, editing pulses at 1.9 (ON), and 7.46 ppm (OFF), MOIST water suppression, 10:40 minutes acquisition time). The measured voxel is located in the occipital lobe and has a size of $3 \times 3 \times 3 \text{ cm}^3$. The number of signal averages (NSA) is 320, interleaved in 40 ON/OFF blocks with 8 NSA each. Since individual transients are not accessible in the given data format (.SPAR/.SDAT), one block of 8 NSA is defined as a single transient for the rest of this study. All spectra contain 2048 spectral points with a bandwidth of 2000 Hz.

All files are converted to the NIfTI-MRS format using spec2nii [18]. Free induction decays (FIDs) are preprocessed by applying frequency and phase correction to align the ON and OFF transients using FSL-MRS [4]. This phase and frequency correction is applied within the frequency search range of 1.9 to 4.2 ppm. Next, the data are Fourier transformed and normalized by dividing the magnitude spectrum by its maximum. The ON and OFF and the real and imaginary parts of the spectra are split into separate dimensions for further use in DL models, making the dimensions for one subject: (20, 2, 2, 2048) where the dimensions represent the number of transients, ON/OFF channel, real/imaginary channel, and number of spectral points, respectively. The dataset was split at the subject level into training (70%), validation (15%), and test (15%) sets using stratified sampling based on diagnostic group (healthy control, type 2 diabetes, metabolic syndrome). All transients from a given subject were assigned exclusively to a single split. No explicit quality-based exclusion is performed, as minor imperfections such as suboptimal water suppression or mild instabilities are intentionally retained to reflect realistic in-vivo conditions. Visual inspection confirmed that no spectra contained severe artifacts that could compromise analyses.

2.2 VAE Model

A VAE is used to model and generate complex-valued MRS spectra by learning a low-dimensional latent representation of the spectral data. The VAE is an unsupervised DL model consisting of two neural networks (NNs): an encoder $Q(Z|X)$ and a decoder $P(X|Z)$. The encoder maps an input spectrum X to a latent representation Z , while the decoder reconstructs the spectrum as \hat{X} from samples drawn from the latent space. MRS spectra are inherently complex-valued and consist of real and imaginary components. Both components are treated as separate input channels and are used simultaneously in all loss computations. Each spectrum therefore has the form

$$X = (X^{\text{Re}}, X^{\text{Im}}),$$

with corresponding decoder outputs $\hat{X} = (\hat{X}^{\text{Re}}, \hat{X}^{\text{Im}})$. Each component contains N spectral points, such that

$$X^{\text{Re}} = (x_1^{\text{Re}}, \dots, x_N^{\text{Re}}), \quad X^{\text{Im}} = (x_1^{\text{Im}}, \dots, x_N^{\text{Im}}),$$

and analogously for \hat{X}^{Re} and \hat{X}^{Im} . All subsequent loss computations are applied to both channels simultaneously.

2.2.1 Loss Function

The model is trained by minimizing a total loss that combines a reconstruction term and a latent regularization term:

$$\mathcal{L}_{total} = \mathcal{L}_{recon}(X, \hat{X}) + \beta_{KL} \mathcal{L}_{reg}(Q(Z|X), P(Z)) \quad (1)$$

where \mathcal{L}_{recon} measures the reconstruction fidelity, \mathcal{L}_{reg} penalizes deviations of the latent distribution from a prior $P(Z)$, and β_{KL} controls the relative contribution of the regularization term. Latent regularization is achieved using the standard Kullback-Leibler (KL) divergence between the approximate posterior $Q(Z|X)$, parameterized by $(\mu, \log \sigma^2)$, and an isotropic Gaussian prior $P(Z) = \mathcal{N}(0, I)$. Mathematically, this can be written as

$$\mathcal{L}_{reg}(Q(Z|X), P(Z)) = -\frac{1}{2} \sum_{j=1}^d (1 + \log \sigma_j^2 - \mu_j^2 - \sigma_j^2), \quad (2)$$

with d the dimensionality of the latent space. This term encourages a smooth, well-structured latent space suitable for generative sampling.

Reconstruction accuracy is enforced using a weighted point-wise loss designed to capture metabolite peaks, macromolecule (MM) and baseline contributions, as well as residual lipid and water signals. This loss combines mean squared error (MSE) and L1 terms, with higher weights assigned to the primary spectral region of interest and lower weights elsewhere. With the spectral axis in ppm defined as (p_1, \dots, p_N) for a spectrum with N points, a per-point weighting factor is defined as:

$$w_i = \begin{cases} w_{high}, & p_{min} \leq p_i \leq p_{max} \\ w_{low}, & \text{otherwise,} \end{cases} \quad (3)$$

where (p_{min}, p_{max}) defines the weighted spectral region (set to 0–7 ppm in this work), w_{high} is the weight used within this range, and w_{low} is the weight applied outside this region. Using these weights, the point-wise loss is defined as:

$$\mathcal{L}_{points}(X, \hat{X}) = \alpha_{L2} \frac{1}{N} \sum_{i=1}^N w_i (\hat{x}_i - x_i)^2 + \alpha_{L1} \frac{1}{N} \sum_{i=1}^N w_i |\hat{x}_i - x_i| \quad (4)$$

where α_{L2} and α_{L1} control the relative contribution of the MSE and L1 terms, respectively. The MSE term promotes accurate reconstruction of dominant peaks but can overemphasize large-amplitude deviations, whereas the L1 term provides a more uniform penalty across residuals. Their combination balances peak fidelity with robust reconstruction of lower-amplitude spectral structure. While this point-wise loss emphasizes accurate modeling of the signals of interest, it does not constrain the structure of the residual signal ($r = \hat{X} - X$). Structured residuals may indicate systematic reconstruction errors, such as baseline distortions or unresolved spectral features. To mitigate this, a fast Fourier transform (FFT)-based residual loss is introduced. Although the residual r is already represented in the frequency domain, we compute the FFT, denoted by $\mathcal{F}(\cdot)$, of the complex residual and evaluate the variance of its magnitude, $\sigma_{|\mathcal{F}(r)|}^2$. This metric penalizes coherent or periodic structure across spectral indices rather than random noise, thereby encouraging the residual to be noise-like instead of exhibiting low- or high-frequency patterns that may indicate systematic reconstruction errors. Therefore, the final reconstruction loss is defined as

$$\mathcal{L}_{recon}(X, \hat{X}) = \mathcal{L}_{points}(X, \hat{X}) + \alpha_{\mathcal{F}} \sigma_{|\mathcal{F}(r)|}^2, \quad (5)$$

where $\alpha_{\mathcal{F}}$ controls the relative contribution of the FFT-based residual loss.

2.2.2 Model Architecture

The model architecture consists of symmetric encoder and decoder networks built from fully connected layers. Each input spectrum is represented as a complex-valued signal with length $N = 2048$ points, stored as two channels corresponding to the real and imaginary parts. Before entering the encoder, one transient of either the ON or OFF channel is selected.

During training, data augmentation is applied in the form of random frequency and phase shifts to enhance training data variability and improve robustness to small spectral variations. Phase shifts are sampled from a normal distribution with a standard deviation of $\pi/4$ radians, and frequency shifts are sampled from a normal distribution with a standard deviation of 10 Hz, applied along the spectral axis. The two-channel spectra are then flattened into a single vector of dimension $2N = 4096$. Three fully connected layers in the encoder map this input vector into a low-dimensional latent representation. The decoder mirrors the encoder, expanding the latent vector back into the spectral domain. An overview of the model architecture is shown in Figure 1.

The model is trained using the Adam optimizer with a learning rate scheduler that reduces the learning rate when the validation loss is not improving for 10 epochs. Early stopping is applied if the validation loss does not improve for 30 epochs. Training is performed on a Linux cluster node with 64 CPU cores and one NVIDIA H100 GPU, using Python 3.11.14. The total training time for the final model is approximately 6.5 minutes. The complete configuration, including data preprocessing, model architecture, training procedure, and loss parameters, is provided in the accompanying public GitHub repository (see Code Availability statement).

2.3 Data Generation

Once the VAE model has been trained, new data can be generated. Three different methods are used for the generation of new data, which involves the manipulation of encoded spectra within the latent space. A comprehensive overview of the entire process is presented in Figure 2.

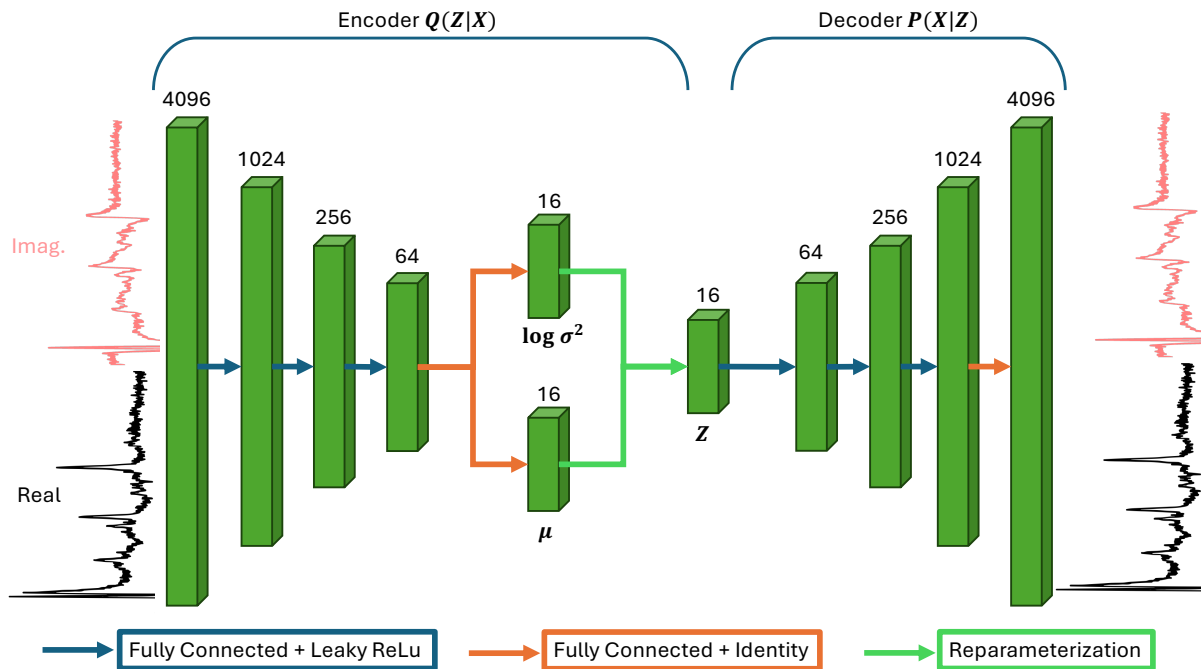


Figure 1: Overview of the used model architecture. Real and imaginary parts of the spectrum are concatenated and used as input for a fully connected NN

The first data generation technique involves random sampling in the learned latent space. In this method, in-vivo spectra are first encoded into latent vectors using the encoder NN, and then random Gaussian noise is added to these latent vectors to produce variations. The perturbed latent vectors are subsequently decoded to generate new spectra. In this study, the Gaussian noise has a mean of 0 and a standard deviation of 0.1. This approach allows controlled variation around in-vivo spectra while remaining rooted in their underlying distribution, as visualized in Figure 2.

Another technique is interpolation. Encoded latent vectors are obtained by encoding in-vivo spectra with the encoder NN. New latent vectors are then generated by linear interpolation along each dimension between pairs or groups of encoded vectors. Decoding these interpolated vectors produces spectra that show gradual transitions in the features present in the original data. Linear interpolation is used in this study for all latent vector dimensions.

The final technique is a hybrid method that combines interpolation with random perturbations. Interpolated latent vectors are perturbed with Gaussian noise (using the same parameters as in the random sampling procedure) before decoding, thereby increasing the diversity of the generated spectra while still remaining anchored in the distribution of in-vivo spectra. All parameters for random perturbation, interpolation, and hybrid sampling, including Gaussian noise magnitudes and interpolation settings, are also provided in the accompanying public GitHub repository (see Code Availability statement).

2.4 Evaluation

2.4.1 Generative Performance

The generative capabilities of the developed VAE model are evaluated by assessing both the reconstruction quality of in-vivo spectra and the similarity between in-vivo and synthetic spectra. Reconstruction performance is examined through visual inspection and by comparing the signal-to-noise ratio (SNR) and linewidth metrics between the in-vivo test spectra and their corresponding reconstructions. The SNR is defined as the ratio between the maximum amplitude

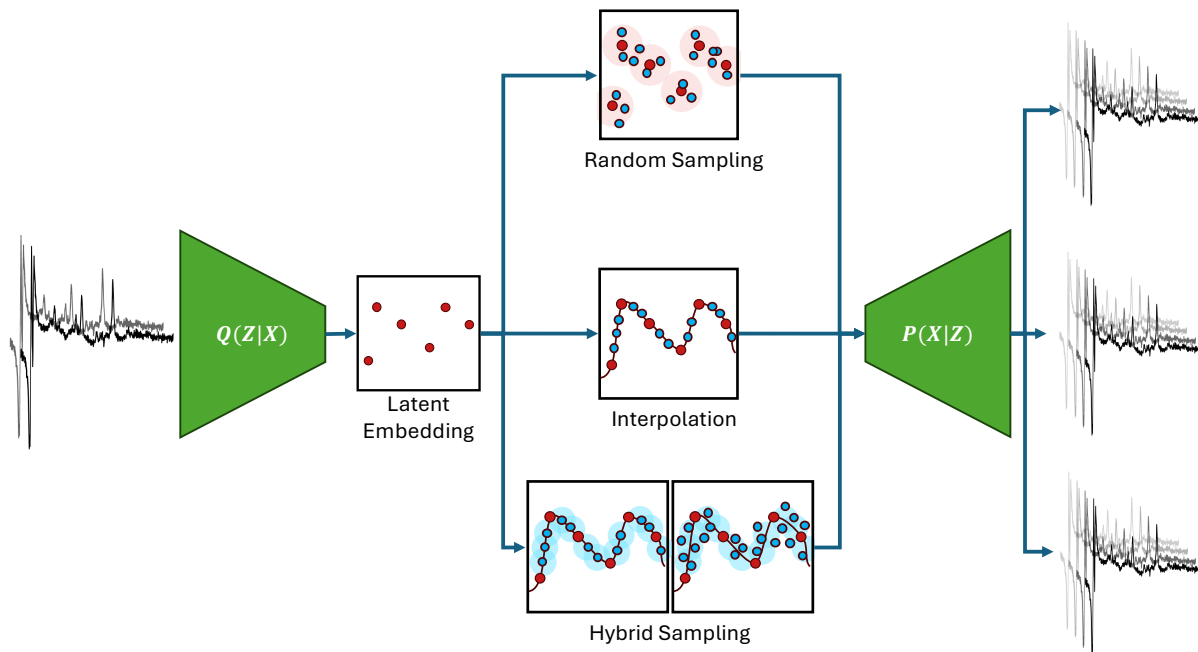


Figure 2: Overview of the data generation pipeline. Real, in vivo spectra are first encoded into latent space. New samples are then generated using one of three methods: random sampling, interpolation, or hybrid sampling. Finally, all generated samples are decoded back into spectra.

of the creatine (Cr) resonance at approximately 3.0 ppm and twice the standard deviation of the spectral noise. Noise is estimated from a metabolite-free region between 9.8 and 10.8 ppm after removal of slow baseline trends using a second-order polynomial fit. The linewidth is defined as the full width at half maximum (FWHM) of the same Cr resonance.

Synthetic samples are subsequently generated from the test set using the three data-generation strategies described in Section 2.3. To assess feature-level similarity between in-vivo and synthetic spectra, uniform manifold approximation and projection (UMAP)[19] is employed. All ON and OFF transients from the in-vivo test set are first used to train the UMAP model and obtain a two-dimensional embedding of the complex spectra. Next, for each generation strategy, the synthetic spectra are projected into the same embedding space using the trained UMAP model. Comparison of the resulting overlap and distribution of data points provides a measure of how well the synthetic spectra capture the feature characteristics of the in-vivo data.

2.4.2 Application-based evaluation

In addition to the previously described evaluations, the practical usability of the generative model is demonstrated through a proof-of-concept application. The application, shown in Figure 3, focuses on spectral reconstruction of γ -aminobutyric acid (GABA)-edited spectra. The aim is to reduce scan time while maintaining spectral quality and quantitative accuracy by artificially increasing the number of transients using generative DL.

The procedure begins with all transients from a single test subject, from which a subset of n transients is selected. These subsets are obtained using a sliding-window technique that selects consecutive, non-overlapping transients to preserve the temporal relationships among them. Each subset is then encoded using the encoder NN, and the resulting latent vectors are used to generate synthetic samples in latent space. These synthetic samples are subsequently decoded using

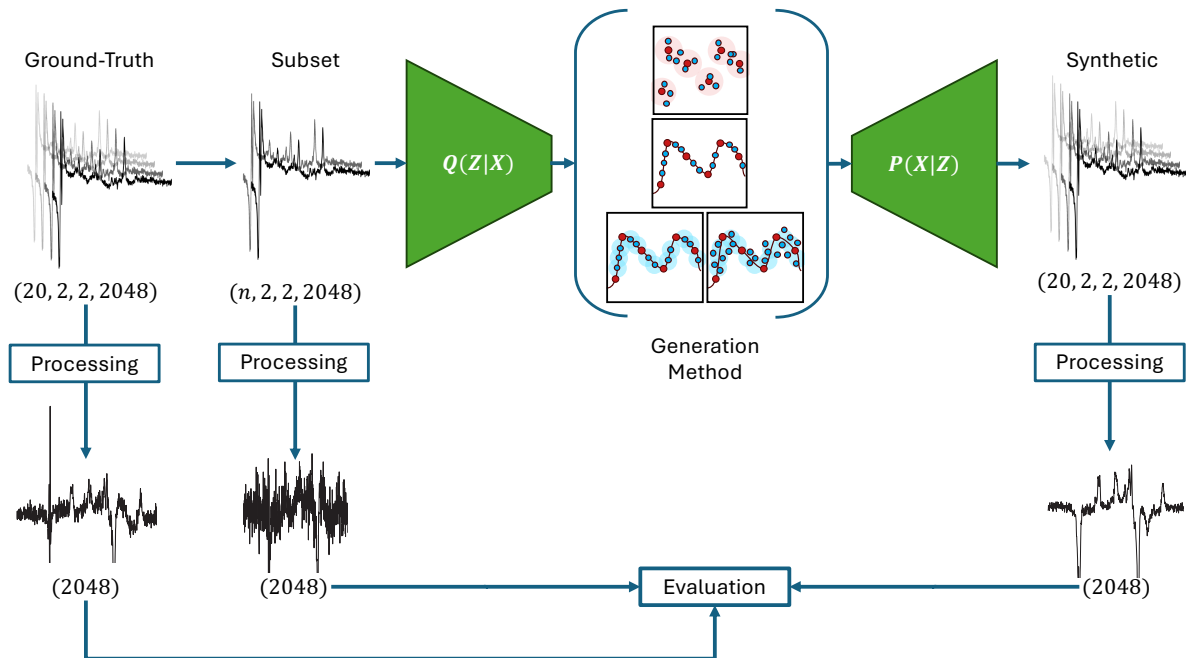


Figure 3: Overview of the application-based evaluation method. Ground truth (GT) spectra from a single subject are used to select a subset of n transients. These transients are encoded using the encoder NN and used for the generation of synthetic samples. The decoder NN generates synthetic transients to end up with the same number of transients as in the GT spectra. For the evaluation all three datasets are processed and fitted using Osprey.

the decoder NN to create a synthetic dataset. In this study, n is set to 2. For each subset, 36 synthetic transients are generated (2×18 , ON and OFF), and the corresponding original in-vivo transients are added, resulting in a total of 40 transients per subject that matches the ground-truth dataset.

After generation, the ground truth, subset, and synthetic spectra are processed in Osprey [20] to obtain GABA-edited difference spectra. The efficacy of the VAE model in this context is assessed by comparing the SNR, linewidth, MSE, and the GABA and glutamate + glutamine (Glx) shape scores of all difference spectra. These selected metrics follow those used in the ISBI Edited MRS Reconstruction Challenge, as described by Berto et al. [21], and all focus on the GABA and Glx peaks. Statistical significant differences between the calculated metrics are determined using a pairwise Wilcoxon Signed-Rank test. Finally, Osprey is used to fit the spectra and to compare GABA and Glx concentrations from the difference spectra, as well as total NAA (tNAA) and total creatine (tCr) concentrations from the OFF spectra. Since no water reference is available for the synthetic data, the amplitudes from the fitting model will be used for comparison. After generation, the ground truth, subset, and synthetic spectra are processed in Osprey [20] to obtain GABA-edited difference spectra. The efficacy of the VAE model in this context is assessed by comparing the SNR, linewidth, MSE, and the GABA and Glx shape scores of all difference spectra. These selected metrics follow those used in the ISBI Edited MRS Reconstruction Challenge, as described by Berto et al. [21], and all focus on the GABA and Glx peaks. Statistical significant differences between the calculated metrics are determined using a pairwise Wilcoxon Signed-Rank test. Finally, Osprey is used to fit the spectra and to compare GABA and Glx concentrations from the difference spectra, as well as tNAA and tCr concentrations from the OFF spectra. Since no water reference is available for the synthetic data, the amplitudes from the fitting model will be used for comparison. Any residual water signal is removed by Osprey prior to metabolite fitting, ensuring that remaining water components do not influence quantification. All Osprey job-file settings are provided in appendix B.

3 Results

All results are obtained using the final model configuration described in the Section 2.2. The complete set of hyperparameters and implementation details is publicly available in the accompanying GitHub repository.

3.1 Generative Performance

Figure 4 illustrates representative examples of in-vivo spectra together with their corresponding reconstructions and residuals. Spectra from two different subjects are shown, each including both OFF and ON transients. These examples are selected as representative of the overall reconstruction performance. Visual inspection of the top two spectra (OFF and ON) shows small and relatively flat residuals, indicating good reconstruction quality. Only minor deviations are observed around the residual water signal. The bottom two spectra exhibit slightly larger residual amplitudes, again predominantly near the water resonance. Importantly, in all cases the residuals do not show structured spectral patterns, suggesting that the reconstruction error is primarily driven by stochastic noise rather than systematic modeling errors.

Quantitative analysis confirms this observation. The reconstruction SNR is consistently higher than the in-vivo SNR, with values of 9.98 ± 1.18 (OFF) and 11.06 ± 1.35 (ON) for the in-vivo spectra, increasing to 17.53 ± 8.36 (OFF) and 19.05 ± 9.01 (ON) for the reconstructed spectra. This SNR increase is consistent with the visual appearance in Figure 4 and reflects that the VAE model suppresses high-frequency noise components rather than reproducing individual noise realizations present in the in-vivo data.

In contrast, the Cr linewidths are well preserved by the reconstruction process. The in-vivo linewidths are 0.057 ± 0.017 ppm (OFF) and 0.062 ± 0.018 ppm (ON), compared to 0.057 ± 0.019 ppm (OFF) and 0.063 ± 0.017 ppm (ON) for the reconstructed spectra. This close agreement indicates that the spectral lineshapes are accurately reconstructed despite the reduction in noise.

Figure 5 shows the UMAP visualizations comparing the three data generation methods with the GT in-vivo dataset. To limit visual clutter, only synthetic spectra generated from a single subset of transients are shown. Across all panels, distinct clusters corresponding to individual subjects are observed. The synthetic spectra largely overlap with the in-vivo data, indicating a high degree of feature similarity between synthetic and real spectra in the embedded space. No pronounced differences between the generation methods are observed. Methods that incorporate random sampling of latent vectors show, at most, a slightly increased spread in the UMAP space.

3.2 Application-based evaluation

Figure 6 compares the spectra generated by the different methods for two representative subjects and subsets of transients. In the top row (a–c), generating additional transients using the VAE results in an increased SNR compared to the original window-based spectra. Consequently, the GABA and Glx peaks in the difference spectrum (Figure 6c) are more pronounced and more comparable to the GT spectrum for all three generative methods.

In contrast, the bottom row (d–f) shows a case in which the spectra generated by the VAE-based methods deviate from the GT. In this example, the OFF, ON, and difference spectra generated by all three methods exhibit increased noise and reduced agreement with the GT compared to the example shown in the top row. Moreover, the synthetic spectra exhibit an N-acetylaspartate (NAA) signal (~ 2 ppm) in the ON acquisition (Figure 6e), which is not expected for this experiment.

Figure 7 presents a quantitative comparison of the metrics introduced in Section 2.4.2, calculated from the difference spectra. For the SNR and linewidth metrics, the corresponding GT values are included as reference. In general, each boxplot comprises 16 subjects across 10 subsets of transients, resulting in 160 datapoints, except for the GT. In some cases, the linewidth could not be reliably calculated, leading to a reduced number of datapoints for this metric

Across all metrics, statistically significant differences are observed between the window-based spectra and all three data generation methods. In addition, significant differences are observed between the generative methods themselves, with a lower MSE for the hybrid method compared to interpolation, and lower SNR and shape scores for the interpolation method compared to both random sampling and hybrid generation.

In Figures 8 and 9, the quantification results for the OFF and difference spectra are shown as heatmaps, indicating the relative concentration error with respect to the GT test spectra. For each subject, the relative error is reported per subset of transients, and the corresponding mean absolute relative error (MARE) across all subsets is summarized in an adjacent column. The MARE values shown in bold indicate the method yielding the lowest average deviation from the GT quantification for that subject.

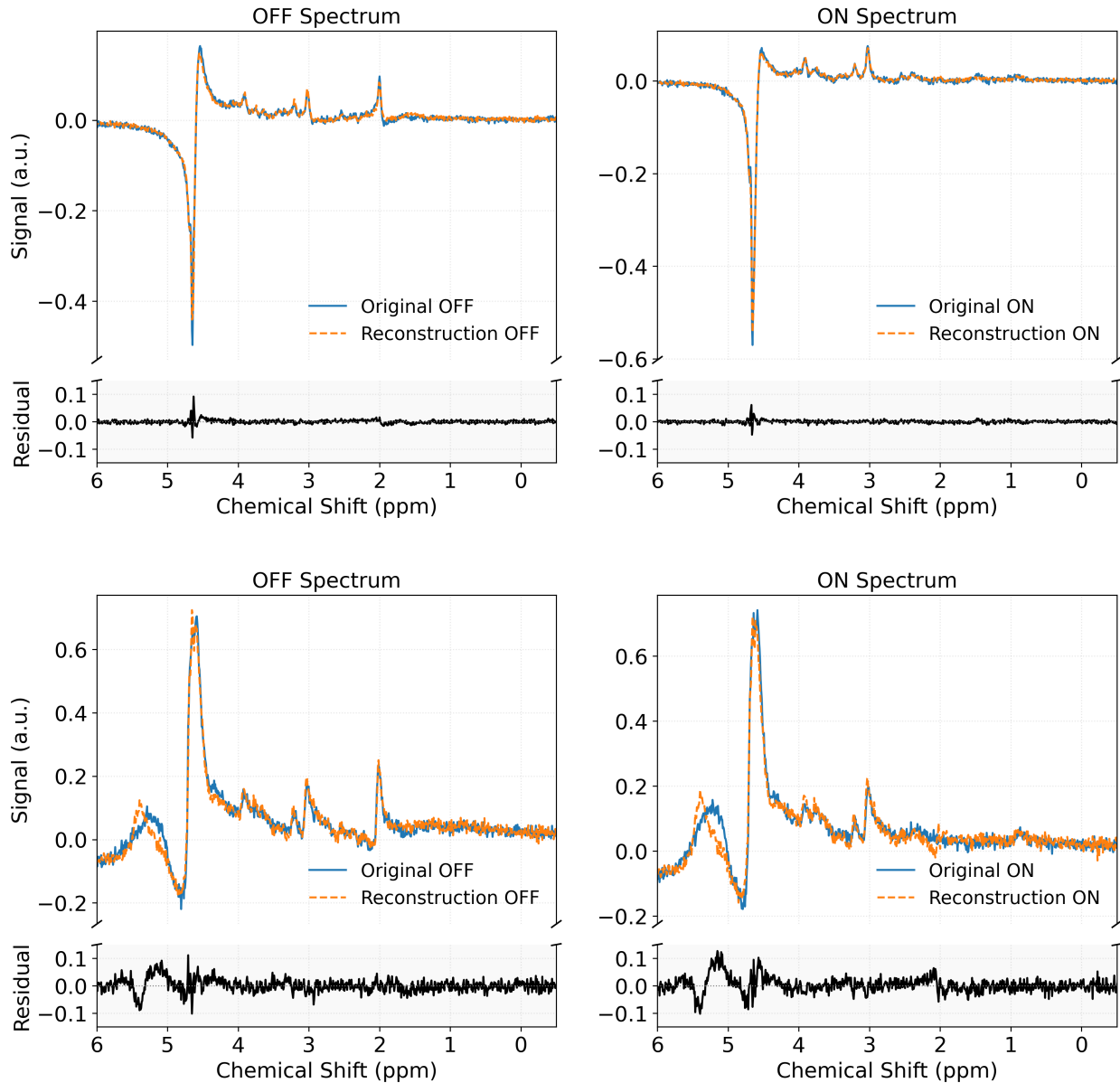


Figure 4: Representative in-vivo spectra (blue) and corresponding reconstructions (orange) with residuals (black) for two subjects. Top panels show OFF and ON spectra with small, flat residuals, indicating accurate reconstruction. Bottom panels show another subject with slightly larger residuals, primarily around the water signal, while the overall spectral shapes are preserved.

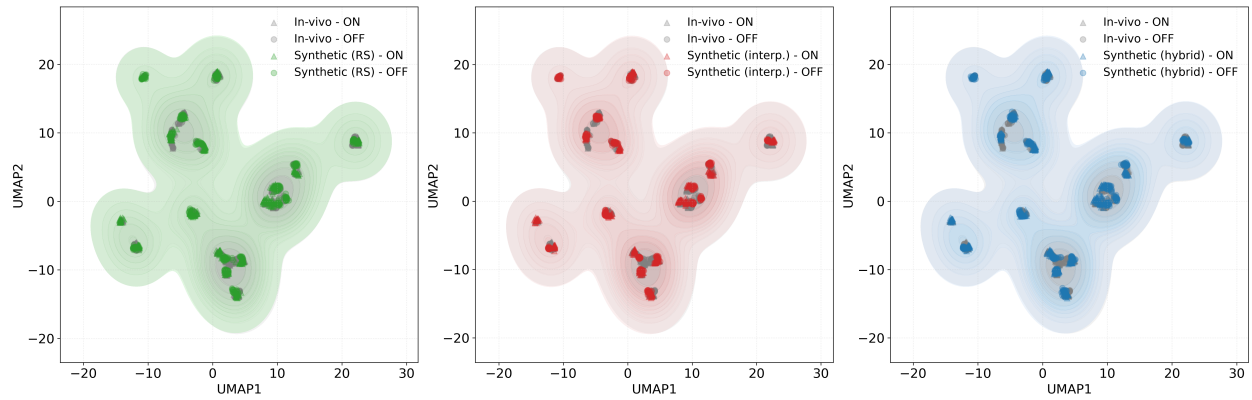
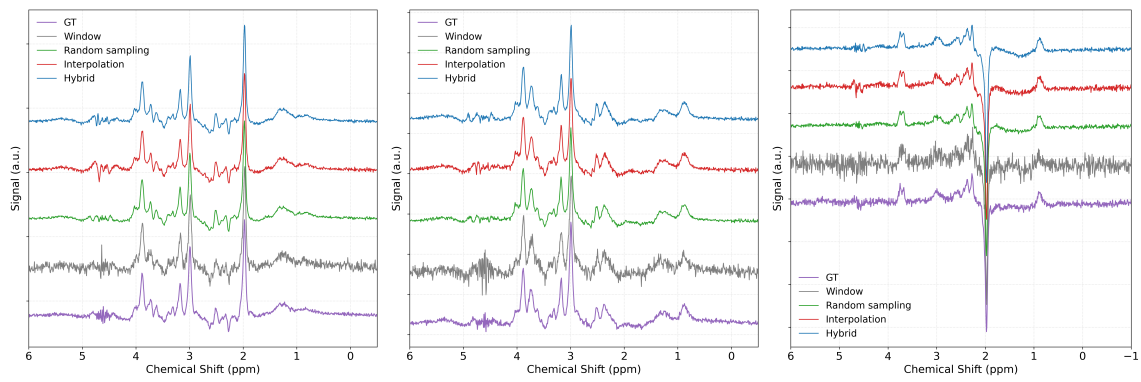
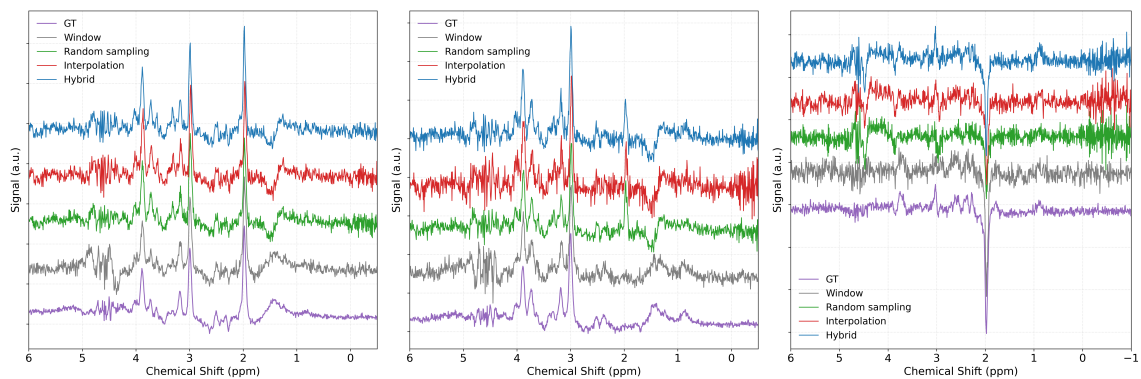


Figure 5: UMAP visualizations comparing GT in-vivo spectra with synthetic spectra generated using three different data generation methods: random sampling (RS) (green), interpolation (red), and hybrid sampling (blue). The UMAP embedding is learned using the GT data, after which synthetic spectra generated from a single subset of transients are projected into the same low-dimensional space. Each point represents an individual spectrum, with markers indicating ON and OFF acquisitions. The shaded regions represent kernel density estimates of the embedded spectral distributions for both GT and synthetic data, illustrating the overall spatial extent and degree of overlap between datasets. Clusters corresponding to individual subjects are visible across all panels.



(a) OFF spectra for all methods, subject C008. (b) ON spectra for all methods, subject C008. (c) Difference (OFF-ON) spectra for all methods, subject C008.



(d) OFF spectra for all methods, subject C039. (e) ON spectra for all methods, subject C039. (f) Difference (OFF-ON) spectra for all methods, subject C039.

Figure 6: Comparison of OFF, ON, and difference (OFF-ON) spectra across different data generation methods for two representative subjects. The top row (a-c) shows spectra from subject C008 (subset transient #6), and the bottom row (d-f) shows spectra from subject C039 (subset transient #6). For each subject, OFF spectra, ON spectra, and the corresponding difference spectra are shown from left to right.

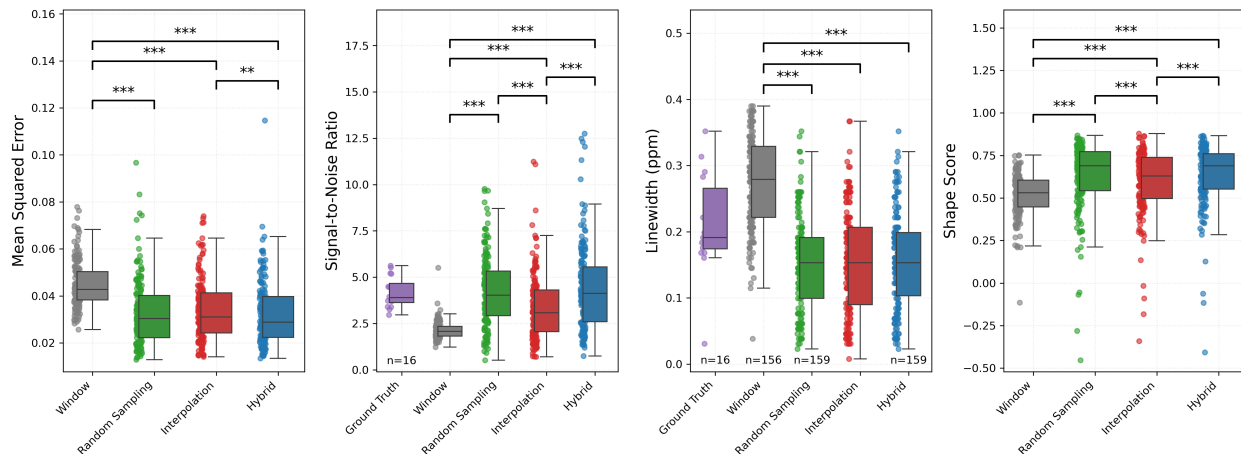


Figure 7: Overview of quantitative metrics for the selected windows (gray) and the different data generation methods: random sampling (green), interpolation (red), and hybrid generation (blue). Metrics are computed from the difference spectra. For the SNR and linewidth metrics, GT values are shown as reference. Statistically significant differences are indicated (***) $p < 0.001$, ** $p < 0.01$, * $p < 0.05$). Boxplots with fewer than the nominal $16 \times 10 = 160$ datapoints are explicitly marked.

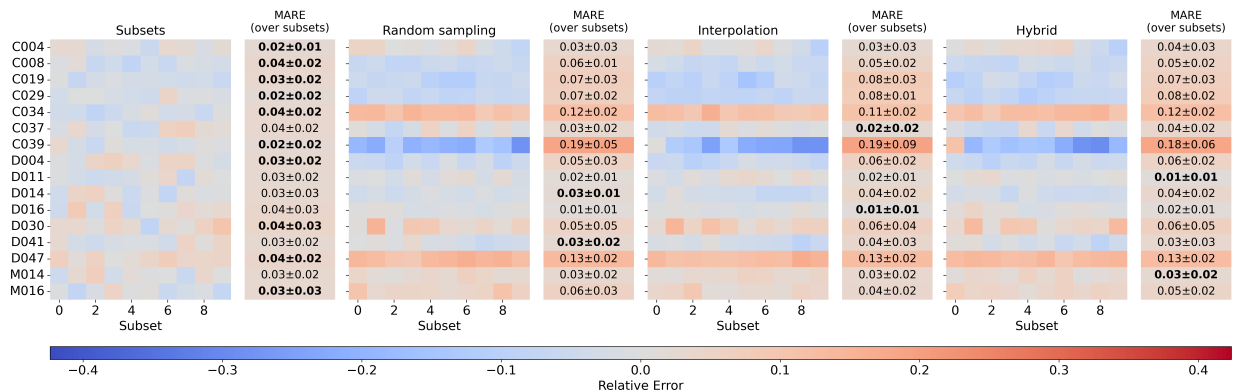
Figure 8 shows the quantification results for the tNAA and tCr metabolites derived from the OFF spectra. For tNAA, the relative errors are generally small across subjects and subsets of transients, with most values remaining close to zero. Nevertheless, for all three generative methods, several subjects and subsets exhibit larger deviations. In particular, subject C039 shows repeated underestimations of the GT amplitudes across subsets, while subjects C034 and D047 display more pronounced overestimations. When summarizing the errors across subsets, the lowest MARE values are most frequently observed for the original subset-based spectra. A similar pattern is observed for tCr, for which the subset-based spectra again yield the lowest MARE values, whereas the generative methods tend to show systematic overestimations and increased variability.

The quantification results for the difference spectra are shown in Figure 9 for the Glx and GABA metabolites. For Glx, the original subsets again result in the lowest MARE values for most subjects, although for specific subjects and subsets the generative methods achieve lower relative errors. The relative errors for GABA are larger compared to the other metabolites. Even for the original subset-based spectra, substantial deviations are present, with relative errors exceeding 1.0 for several subsets. While the MARE values remain high overall, the generative methods yield quantification results that are closer to the GT for a majority of subjects, with the interpolation and hybrid approaches each producing the lowest MARE values for five subjects, and the random sampling approach for two subjects. For both Glx and GABA, subject C039 again exhibits the largest deviations for the generative methods, consistent with the observations for the OFF spectra.

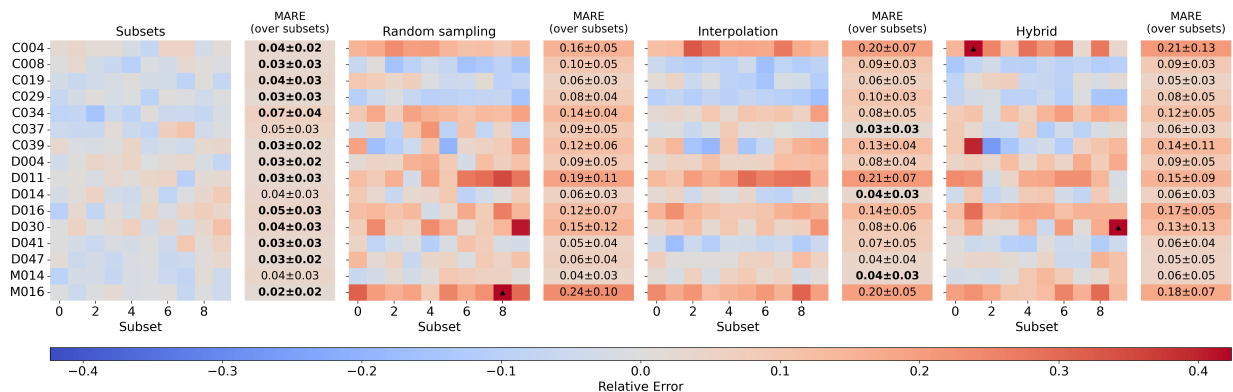
4 Discussion

The developed VAE model accurately reconstructs the dominant spectral patterns present in MRS data, but it has difficulty capturing stochastic components. In particular, the model does not accurately reproduce noise, which is consistent with its learning objective. During training, the VAE is optimized to encode and reconstruct systematic and recurrent spectral features, which are represented in the latent space. Random noise, by definition, lacks consistent structure across the spectral range and therefore cannot be effectively encoded. As a result, the decoder primarily reconstructs the underlying signal while largely suppressing stochastic fluctuations. This behavior is reflected in the comparable linewidths but differing SNR levels between the in-vivo and reconstructed spectra, as shown in Section 3.1. Importantly, this limitation does not reduce the practical usefulness of the generated data if lower SNR is required, since noise can be added post-hoc to achieve desired SNR levels in a controlled manner.

A similar reconstruction challenge is observed for the residual water signal. Although this signal is not inherently stochastic, its amplitude, phase, and lineshape vary substantially across the dataset due to differences in water suppression efficiency and local field conditions, and its presence is not consistent across all spectra. In contrast to metabolite resonances, which are constrained by fixed chemical shifts and coupling patterns, residual water exhibits a much larger dynamic range and less structured variability, making it more difficult for the model to reproduce consistently.



(a) tNAA quantification results for the OFF spectra.

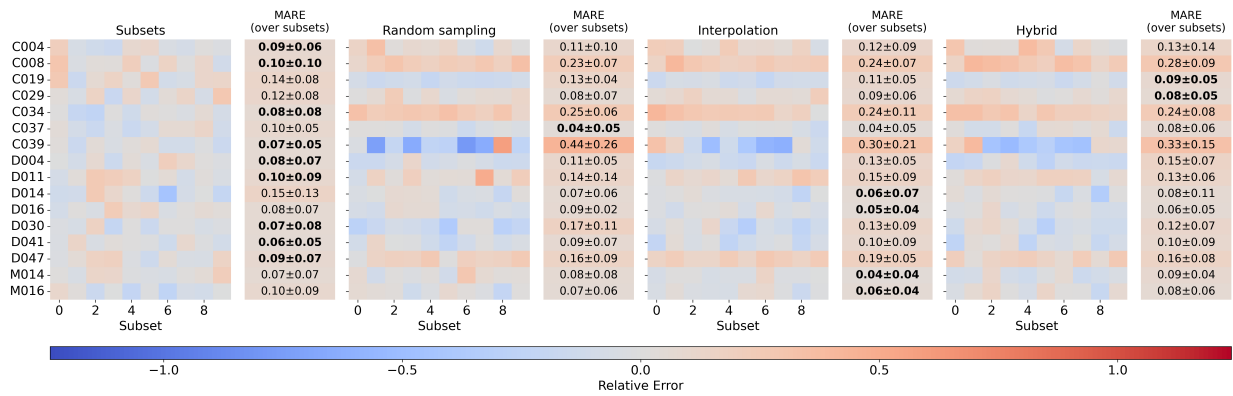


(b) tCr quantification results for the OFF spectra.

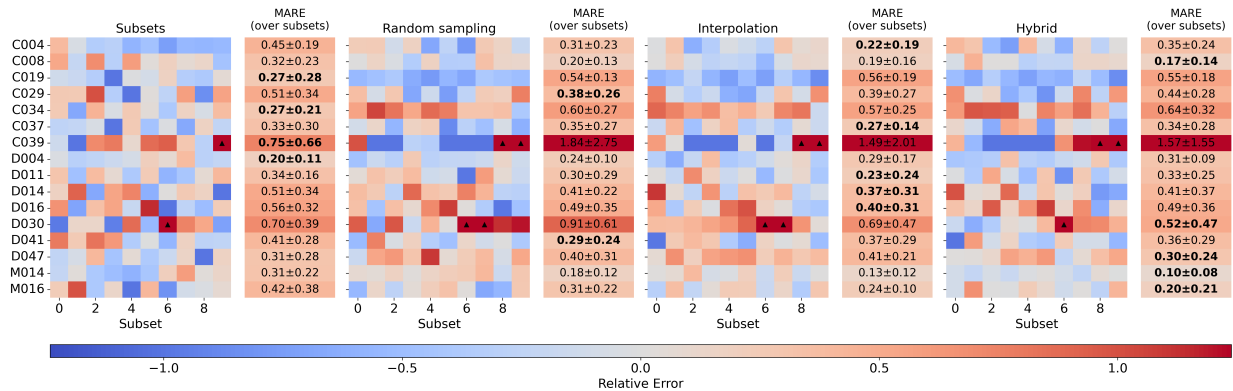
Figure 8: Heatmaps showing the relative concentration error with respect to the GT test spectra for the OFF spectra. For each subject, the relative error is shown per window for the different reconstruction methods. The adjacent column summarizes the MARE across all windows for each subject. Values printed in bold indicate the method yielding the lowest MARE for that subject. The color scale is shared across methods. The ▲ symbols indicate values that exceed the displayed range.

Consequently, the residual water component is not reliably reconstructed in all cases, as illustrated in Figure 4. Despite these imperfections, the synthetic spectra preserve the essential characteristics of the in-vivo data. As shown in Figure 5, the generated spectra occupy the same low-dimensional feature space as the in-vivo spectra, indicating that the VAE captures the global metabolite-driven spectral structure of the in-vivo data, even though stochastic noise characteristics and artifact-related variability (e.g., baseline distortions or residual water) are not fully reproduced.

The UMAP visualizations in Figure 5 further reveal clustering patterns corresponding to individual subjects in the dataset. While most subjects form clearly separated clusters in both the in-vivo and synthetic data, some datapoints lie in close proximity and partially overlap, indicating high feature similarity. This observation is particularly relevant for the random latent-space sampling strategy used to generate synthetic spectra. Assuming that spectra with similar structure are located near each other in latent space, excessive perturbations during sampling may cause transitions across cluster boundaries. As a result, features from different conditions—such as ON and OFF spectra, or even spectra from different subjects—may become inadvertently mixed. An example of this effect is shown in Figure 6e, where synthetic ON spectra exhibit a detectable NAA signal that is not expected to be present. Although this behavior is not observed consistently across all subjects, it highlights the importance of carefully controlling latent-space sampling and implementing appropriate quality control when synthetic spectra are used in downstream processing pipelines.



(a) Glx quantification results for the difference spectra.



(b) GABA quantification results for the difference spectra.

Figure 9: Heatmaps showing the relative concentration error with respect to the GT test spectra for the difference spectra. For each subject, the relative error is shown per subset of transients for the different reconstruction methods. The adjacent column summarizes the MARE across all subsets for each subject. Values printed in bold indicate the method yielding the lowest MARE for that subject. The color scale is shared across methods. The \blacktriangle symbols indicate values that exceed the displayed range.

A strength of the proposed approach is its ability to model heterogeneous data within a single generative framework. The VAE is trained jointly on spectra from different subject groups (diabetes, metabolic syndrome, and healthy controls) as well as ON and OFF transients, yet was still able to capture meaningful spectral structure. This is reflected in both the qualitative reconstructions and the overlap between in-vivo and synthetic spectra in the UMAP feature space, as well as in the application-based metrics. These findings suggest that the model does not collapse distinct spectral characteristics despite the increased variability in the training data, and is capable of learning shared representations across conditions.

The application-based evaluation demonstrates improved performance across all assessed signal quality metrics, as shown in Figure 7. The inclusion of synthetic spectra leads to improvements in MSE, SNR, linewidth, and shape score for all three data generation methods when compared to the subset-only approach. These results indicate that augmenting a limited subset of transients with synthetic data can enhance overall spectral quality. However, differences between synthetic and GT spectra are observed for the SNR and linewidth metrics. The discrepancy in SNR is expected, given the previously discussed tendency of the VAE to omit stochastic noise. The observation of reduced linewidth in the synthetic spectra is more notable and likely reflects the fact that the generation process is conditioned on only two transients, preventing the model from capturing frequency variations present across the full acquisition. While this results in visually cleaner spectra, it may bias downstream applications that are sensitive to linewidth or frequency variability.

The final part of the evaluation examines the quantification performance of the OFF and difference spectra derived from the GT and synthetic data. For the OFF spectra, the quantification results for tNAA and tCr (Figure 8) show clear differences between the subset-only spectra and the three synthetic data generation methods. While the subset-only approach yields low relative errors ($\text{MARE} \leq 0.07$, and ≤ 0.04 in most cases), augmenting these subsets with synthetic spectra substantially increases errors, reaching up to 0.24 in the most extreme case. This effect is particularly pronounced for tCr, indicating that augmenting a small subset of transients with synthetic spectra can adversely affect metabolite quantification, despite improvements in signal quality metrics. Although uncertainties in the quantification algorithm and in the definition of the GT concentrations cannot be fully excluded, these results suggest that the VAE does not fully preserve the spectral features required for accurate concentration estimation.

A similar pattern is observed for the difference spectra (Figure 9). The Glx amplitudes obtained from the subset-only spectra are generally closer to the GT values than those derived from synthetic spectra. In contrast, the quantification of GABA remains challenging across all approaches, including the subset-only spectra, reflecting the inherent difficulty of reliable GABA estimation. Taken together, these results highlight that while synthetic data generation can improve spectral appearance and stability, it does not necessarily preserve quantitative metabolite accuracy, particularly for applications that rely on absolute concentration estimates.

Importantly, the synthetic spectra primarily expand interspectral variability and not intersubject variability. With a limited number of subjects used to train the VAE, additional generated spectra do not introduce new biological differences between individuals. Rather, they provide model-based samples that remain constrained to the local spectral manifold of the observed subjects. Consequently, synthetic spectra can enrich spectral level variation within subjects, but they should not be interpreted as increasing the effective biological diversity of the cohort. This distinction is particularly important for analyses that depend on realistic intersubject variation.

Beyond the specific performance characteristics of the proposed VAE, an important contribution of this work lies in the multi-faceted nature of the evaluation strategy applied to generative modeling in MRS. Generative approaches in spectroscopy are often assessed primarily through visual inspection or a limited set of signal quality metrics, which may not fully capture their suitability for downstream applications. In contrast, this study combines spectral reconstruction metrics, low-dimensional feature space analysis, application-based evaluation, and metabolite quantification to assess both the strengths and limitations of the generated data. By explicitly identifying scenarios in which synthetic spectra improve signal characteristics as well as cases where they introduce subtle but consequential deviations, this work underscores the necessity of comprehensive, application-aware validation of generative models in spectroscopy.

While the proposed method may not be optimal for applications that require accurate absolute metabolite quantification, the ability to generate realistic spectra conditioned on limited input data may be advantageous for other downstream tasks. In particular, generative augmentation could be used to balance or oversample specific classes in classification settings, where relative spectral differences and shared structure are more important than precise concentration estimates. Such applications could benefit from the increased data diversity provided by synthetic spectra without requiring strict preservation of absolute metabolite levels. However, the dataset used in this study is not well suited for evaluating this scenario, as differences between subject groups are subtle at the level of individual spectra and primarily become apparent only when aggregating results at the group level [17]. Exploring the potential of the proposed approach for classification or other discriminative tasks therefore remains an important direction for future work.

5 Conclusion

In this study, we developed a VAE-based generative model capable of synthesizing realistic proton brain MRS spectra, capturing the dominant spectral patterns of an in-vivo dataset in low-dimensional features. The model preserves global spectral characteristics, as confirmed by reconstruction performance, UMAP embeddings, and quantitative metrics, and it improves signal quality metrics across multiple synthetic data generation approaches. However, limitations remain, including inconsistent reconstruction of stochastic components such as noise and residual water signals, as well as reduced accuracy in metabolite quantification. Beyond these specific results, this work demonstrates a comprehensive evaluation framework for generative MRS models, highlighting both their potential to augment datasets and the importance of careful validation for quantitative or downstream analyses. Future studies could explore these applications further, and extend the model to larger datasets or alternative acquisition schemes, building on this framework. Together, these results provide a foundation for the responsible and effective use of generative AI in MRS research.

References

- [1] Dicheng Chen, Zi Wang, Di Guo, Vladislav Orekhov, and Xiaobo Qu. Review and prospect: Deep learning in nuclear magnetic resonance spectroscopy. *Chemistry – A European Journal*, 26(46):10391–10401, 2020.
- [2] Dennis M. J. van de Sande, Julian P. Merkofer, Sina Amirrajab, Mitko Veta, Ruud J. G. van Sloun, Maarten J. Versluis, Jacobus F. A. Jansen, Johan S. van den Brink, and Marcel Breeuwer. A review of machine learning applications for the proton MR spectroscopy workflow. *Magnetic Resonance in Medicine*, 90(4):1253–1270, 2023.
- [3] Robin Simpson, Gabriel A. Devenyi, Peter Jezzard, T. Jay Hennessy, and Jamie Near. Advanced processing and simulation of MRS data using the FID appliance (FID-A)—An open source, MATLAB-based toolkit. *Magnetic Resonance in Medicine*, 77(1):23–33, 2017.
- [4] William T. Clarke, Charlotte J. Stagg, and Saad Jbabdi. FSL-MRS: An end-to-end spectroscopy analysis package. *Magnetic Resonance in Medicine*, 85(6):2950–2964, 2021.
- [5] Brian J. Soher, Philip Semanchuk, David Todd, Xiao Ji, Dinesh Deelchand, James Joers, Gulin Oz, and Karl Young. Vespa: Integrated applications for RF pulse design, spectral simulation and MRS data analysis. *Magnetic Resonance in Medicine*, 90(3):823–838, 2023.
- [6] John LaMaster, Georg Oeltzschner, and Yan Li. MRS-Sim: Open-Source Framework for Simulating In Vivo-Like Magnetic Resonance Spectra. *NMR in Biomedicine*, 38(10):e70130, 2025.
- [7] D. M. J. van de Sande, A. T. Gudmundson, S. Murali-Manohar, C. W. Davies-Jenkins, D. Simicic, G. Simegn, İ. Özdemir, S. Amirrajab, J. P. Merkofer, H. J. Zöllner, G. Oeltzschner, and R. a. E. Edden. A Digital Phantom for MR Spectroscopy Data Simulation. *Magnetic Resonance in Medicine*, 95(3):1345–1359, 2026.
- [8] Robert Mulkern and John Bowers. Density matrix calculations of AB spectra from multipulse sequences: Quantum mechanics meets In vivo spectroscopy. *Concepts in Magnetic Resonance*, 6(1):1–23, January 1994.
- [9] Aaron R. Flanagan, Dhairya Dalal, and Frank G. Glavin. Exploring Generative Artificial Intelligence and Data Augmentation Techniques for Spectroscopy Analysis. *Chemical Reviews*, 125(13):6130–6155, July 2025.
- [10] Shuki Maruyama and Hidenori Takeshima. Generating Synthetic MR Spectroscopic Imaging Data with Generative Adversarial Networks to Train Machine Learning Models. *Magnetic Resonance in Medical Sciences*, 24(4):n/a, 2025.
- [11] N. Olliverre, G. Yang, G. Slabaugh, C. C. Reyes-Aldasoro, and E. Alonso. Generating magnetic resonance spectroscopy imaging data of brain tumours from linear, non-linear and deep learning models. In A. Gooya, O. Goksel, I. Oguz, and N. Burgos, editors, *Simulation and Synthesis in Medical Imaging*, volume 11037 of *Lecture Notes in Computer Science*. SASHIMI 2018 / MICCAI Society, Springer, 2018.
- [12] Joon Jang, Hyeong Hun Lee, Ji-Ae Park, and Hyeonjin Kim. Unsupervised anomaly detection using generative adversarial networks in 1H-MRS of the brain. *Journal of Magnetic Resonance*, 325:106936, April 2021.
- [13] Diederik P. Kingma and Max Welling. Auto-encoding variational bayes. <https://arxiv.org/abs/1312.6114>, May 2014. Preprint, arXiv:1312.6114.
- [14] Aghiles Kebaili, Jérôme Lapuyade-Lahorgue, and Su Ruan. Deep Learning Approaches for Data Augmentation in Medical Imaging: A Review. *Journal of Imaging*, 9(4):81, April 2023.
- [15] Khadija Rais, Mohamed Amroune, Abdelmadjid Benmachiche, and Mohamed Yassine Haouam. Exploring variational autoencoders for medical image generation: A comprehensive study. <https://arxiv.org/abs/2411.07348>, November 2024. Preprint, arXiv:2411.07348.
- [16] Miranda T. Schram, Simone J. S. Sep, Carla J. van der Kallen, Pieter C. Dagnelie, Annemarie Koster, Nicolaas Schaper, Ronald M. A. Henry, and Coen D. A. Stehouwer. The Maastricht Study: An extensive phenotyping study on determinants of type 2 diabetes, its complications and its comorbidities. *European Journal of Epidemiology*, 29(6):439–451, June 2014.
- [17] Frank C. G. van Bussel, Walter H. Backes, Paul A. M. Hofman, Nicolaas A. J. Puts, Richard A. E. Edden, Martin P. J. van Boxtel, Miranda T. Schram, Coen D. A. Stehouwer, Joachim E. Wildberger, and Jacobus F. A. Jansen. Increased GABA concentrations in type 2 diabetes mellitus are related to lower cognitive functioning. *Medicine*, 95(36):e4803, September 2016.
- [18] William T. Clarke, Tiffany K. Bell, Uzay E. Emir, Mark Mikkelsen, Georg Oeltzschner, Amirmohammad Shamaei, Brian J. Soher, and Martin Wilson. NIFTI-MRS: A standard data format for magnetic resonance spectroscopy. *Magnetic Resonance in Medicine*, 88(6):2358–2370, 2022.

- [19] Leland McInnes, John Healy, and James Melville. UMAP: Uniform Manifold Approximation and Projection for Dimension Reduction. <http://arxiv.org/abs/1802.03426>.
- [20] Georg Oeltzschner, Helge J. Zöllner, Steve C. N. Hui, Mark Mikkelsen, Muhammad G. Saleh, Sofie Tapper, and Richard A. E. Edden. Osprey: Open-source processing, reconstruction & estimation of magnetic resonance spectroscopy data. *Journal of Neuroscience Methods*, 343:108827, September 2020.
- [21] Rodrigo Pommot Berto, Hanna Bugler, Gabriel Dias, Mateus Oliveira, Lucas Ueda, Sergio Dertkigil, Paula D. P. Costa, Leticia Rittner, Julian P. Merkofer, Dennis M. J. van de Sande, Sina Amirrajab, Gerhard S. Drenthen, Mitko Veta, Jacobus F. A. Jansen, Marcel Breeuwer, Ruud J. G. van Sloun, Abdul Qayyum, Cristobal Rodero, Steven Niederer, Roberto Souza, and Ashley D. Harris. Results of the 2023 ISBI challenge to reduce GABA-edited MRS acquisition time. *Magnetic Resonance Materials in Physics, Biology and Medicine*, April 2024.
- [22] Alexander Lin, Ovidiu Andronesi, Wolfgang Bogner, In-Young Choi, Eduardo Coello, Cristina Cudalbu, Christoph Juchem, Graham J. Kemp, Roland Kreis, Martin Krššák, Phil Lee, Andrew A. Maudsley, Martin Meyerspeer, Vladamir Mlynarik, Jamie Near, Gülin Öz, Aimie L. Peek, Nicolaas A. Puts, Eva-Maria Ratai, Ivan Tkáč, Paul G. Mullins, and Experts' Working Group on Reporting Standards for MR Spectroscopy. Minimum Reporting Standards for in vivo Magnetic Resonance Spectroscopy (MRSinMRS): Experts' consensus recommendations. *NMR in Biomedicine*, 34(5):e4484, 2021.

Code Availability

All code used in this study is publicly available in a GitHub repository. The repository link will be provided upon final publication.

Conflict of interest

The authors declare no potential conflict of interests.

A MRS in MRS

This section provides transparency and reproducibility by adhering to the minimum reporting standards for in-vivo magnetic resonance spectroscopy (MRS) (MRSinMRS) guidelines [22]. The table details the hardware, acquisition, processing, and data quality parameters for this study.

Table 1: Minimum Reporting Standards for in-vivo Magnetic Resonance Spectroscopy (MRSinMRS) [22] for used dataset. Details are retrieved from the data and the work from van Bussel et al. [17]

Header / SubHeader	Values
Site (name or number)	
1. Hardware	
a. Field strength	3T
b. Manufacturer	Philips
c. Model (software version if available)	Achieva TX
d. RF coils: nuclei (transmit/receive), number of channels, type, body part	1H, 32-element, head coil
e. Additional hardware	-
2. Acquisition	
a. Pulse sequence	MEGA-PRESS
b. Volume of interest (VOI) locations	occipital lobe
c. Nominal VOI size	30×30×30 mm ³
d. Repetition time (TR), echo time (TE)	TR = 2000 ms, TE = 68 ms
e. Total number of excitations or acquisitions per spectrum	320, interleaved in 40 blocks
f. Additional sequence parameters	2000 Hz spectral width, 2048 spectral points, editing pulses at 1.9 (ON), and 7.46 ppm (OFF)
g. Water suppression method	MOIST water suppression
h. Shimming method, reference peak, and thresholds for “acceptance of shim” chosen	unknown
i. Triggering or motion correction method	-
3. Data analysis methods and outputs	
a. Analysis software	In-house Python scripts FSL-MRS[4] (2.1.20) Osprey [20] (2.9.6)
b. Processing steps deviating from quoted reference or product	Alignment of dynamics along time dimension (0.2–4.2 ppm); water referencing and eddy current correction (ECC) using reference data; frequency shift to 3.027 ppm reference peak; phase correction over 2.9–3.1 ppm.
c. Output measure	Amplitudes/institutional units
d. Quantification references and assumptions, fitting model assumptions	See Osprey job file in Appendix B
4. Data quality	
a. Reported variables (SNR, linewidth (with reference peaks))	SNR: 9.98 ± 1.18 (OFF) and 11.06 ± 1.35 (ON), FWHM: 0.057 ± 0.017 ppm (OFF) and 0.062 ± 0.018 ppm (ON), all referenced to Cr
b. Data exclusion criteria	-
c. Quality measures of postprocessing model fitting	-
d. Sample spectrum	See Figures 4 and 6

B Example MATLAB Osprey Job Script

```

1
2 %% 1. SPECIFY SEQUENCE INFORMATION
3 seqType = 'MEGA'; % Options: 'unedited', 'MEGA', 'HERMES', '
HERCULES'
4 editTarget = {'GABA'}; % Editing targets
5 dataScenario = 'invivo'; % Options: 'invivo', 'phantom', 'PRIAM', '
MRSI'
6
7 %% 2. DATA HANDLING AND MODELING OPTIONS
8 opts.SpecReg = 'RobSpecReg'; % Spectral registration method
9 opts.SubSpecAlignment.mets = 'L2Norm'; % Sub-spectrum alignment
10 opts.ECC.raw = 1; % Eddy current correction
11 opts.ECC.mm = 1;
12 opts.saveLCM = 0;
13 opts.savejMRUI = 0;
14 opts.saveVendor = 0;
15 opts.saveNII = 1;
16 opts.savePDF = 0;
17 opts.exportParams.flag = 0;
18 opts.exportParams.path = ''; % Path to save parameters
19
20 opts.fit.method = 'Osprey'; % Fitting algorithm
21 opts.fit.includeMetabs = {'default'}; % Metabolites to include
22 opts.fit.style = 'Separate'; % Fit style for edited datasets
23 opts.fit.range = [0.5 4]; % Fitting range [ppm]
24 opts.fit.rangeWater = [2.0 7.4];
25 opts.fit.bLineKnotSpace = 0.55;
26 opts.fit.fitMM = 1; % Include macromolecules/lipids
27 opts.fit.coMM3 = '3to2MM';
28 opts.fit.FWHMcoMM3 = 14;
29 opts.fit.basisSetFile = '/PATH/TO/BASISSET/basis_philips_megapress_gaba68.mat
';
30
31 opts.img.deface = 0; % Optional: deface structural images
32
33 %% 3. SPECIFY MRS DATA AND STRUCTURAL IMAGING FILES
34 clear files files_ref files_w files_nii files_mm
35
36 root = '/PATH/TO/MRS_DATA';
37 model = 'MODEL_NAME';
38 subjects = {};
39 windows = [];
40 types = {'gt', 'window', 'interpolation', 'random_sampling', 'random_interpolation
'};
41
42 files = getNiftiFiles(root, model, subjects, windows, types);
43
44 %% 4. SPECIFY STAT FILE
45 % Not used in this example
46
47 %% 5. SPECIFY OUTPUT FOLDER
48 outputFolder = fullfile('/PATH/TO/OUTPUT', model);
49 if ~exist(outputFolder, 'dir')
50 mkdir(outputFolder);
51 end
52
53 % Save file list
54 fileListTxt = fullfile(outputFolder, 'file_list.txt');
55 fid = fopen(fileListTxt, 'w');
56 for i = 1:length(files)
57 fprintf(fid, '%s\n', files{i});
58 end
59 fclose(fid);

```

Listing 1: Osprey Job script used for the quantification of the in-vivo and synthetic spectra.